Hyperbolic contraction measuring systems for extensional flow

M. Nyström[1], H.R. Tamaddon Jahromi[2], M. Stading[1,3] and M.F. Webster[2]

[1]SP - Technical Research Institute of Sweden, Food and Bioscience, SE-40229 Göteborg, Sweden

[2]Institute of Non-Newtonian Fluid Mechanics, Swansea University, College of Engineering, Fabian Way, Bay Campus, Swansea, SA1 8EN, UK

[3]Department of Materials and Manufacturing Technology, Chalmers University of Technology, SE-412 76 Göteborg, Sweden

Abstract

In this paper an experimental method for extensional measurements on medium viscosity fluids in contraction flow is evaluated through numerical simulations and experimental measurements. This measuring technique measures the pressure drop over a hyperbolic contraction, caused by fluid extension and fluid shear, where the extensional component is assumed to dominate. The present evaluative work advances our previous studies on this experimental method by introducing several contraction ratios and addressing different constitutive models of varying shear and extensional response. The constitutive models included are those of the constant viscosity Oldroyd-B and FENE-CR models, and the shear-thinning LPTT model. Examining the results, the impact of shear and first normal stress difference on the measured pressure drop are studied through numerical pressure drop predictions. In addition, stream function patterns are investigated to detect vortex development and influence of contraction ratio. The numerical predictions are further related to experimental measurements for the flow through a 15:1 contraction ratio with three different test fluids. The measured pressure drops are observed to exhibit the same trends as predicted in the numerical simulations, offering close correlation and tight predictive windows for experimental data capture. This result has demonstrated that the hyperbolic contraction flow is well able to detect such elastic fluid properties, and that this is matched by numerical predictions in evaluation of their flow response. The hyperbolical contraction flow technique is commended for its distinct benefits – it is straightforward and simple to perform, the Hencky strain can be set by changing contraction ratio, non-homogenous fluids can be tested, and one can directly determine the degree of elastic fluid behaviour. Based on matching of viscometric extensional viscosity response for FENE-CR and LPTT models, a decline is predicted in pressure drop for the shear-thinning LPTT model. This would indicate a modest impact of shear in the flow, since such a pressure drop decline is relatively small. It is particularly noteworthy, that the increase in pressure drop gathered from the experimental measurements is relatively high despite the low Deborah number range explored.

Keywords: Hyperbolic contraction, pressure-drop, viscoelastic fluid, Boger fluid, extensional flow, axisymmetric contraction-expansion.

1. Introduction

In a large number of industries, knowledge of flow behaviour of fluids is necessary for appropriate quality control, product development and process design. A common procedure to study flow behaviour is to determine properties like shear viscosity during shear flow. But as soon as a viscoelastic fluid undergoes any sudden geometric change (e.g. contraction or expansion), extensional deformation will occur, generating the need of also determining the extensional viscosity. Many fluids used in industry and most food products are viscoelastic, which means that their extensional response will have an impact on the overall behaviour of the fluid. Since the behaviour in shear and extension can be quite diverse, both shear and extensional properties have to be determined for viscoelastic fluids. Moreover, extensional properties also have a considerable impact on sensory perception - texture and mouth feel of a food product (Chen et al. 2011; Dobraszczyk 2003; Koliandris et al. 2011). Today, there are a number of well-known measuring techniques for determining extensional properties, such as the filament-stretching extensional rheometer (*FiSER*) (Gupta 2000; Meissner 1972), the Meissner elongational melt rheometer (Meissner 1972; Meissner et al. 1997) and the similar SER and EVF, capillary break-up (*CaBER*) (Entov and Hinch 1997) and opposed jets (Fuller et al. 1985). However, none of these techniques are adapted to measure on medium non perfectly homogenous viscosity fluids, which are common in e.g. food products and bio-fluids. The term “medium viscosity fluids” is a loose description of fluids having shear viscosities between polymer melts and dilute solutions, typically 1-1000 Pas. The CaBER mainly covers the low viscosity range and the FiSER requires liquids which are possible to extend to long and thin filaments. Moreover, most food and bio-fluids are not perfectly homogeneous and do not form perfect filaments. In addition, only the capillary break-up method, and the wind-up methods (SER, EVF) are available commercially.

The hyperbolic contraction flow (HCF) developed by Wikström and Bohlin (1999) and Stading and Bohlin (2000, 2001) is a proposed measuring technique specially aimed for these medium viscosity fluids. The system can be mounted into any commercially available tension tester where a controlled deformation and deformation rate can be set, and the resulting force is measured. The HCF is based on contraction flow, where the fluid is forced through a hyperbolic nozzle at constant displacement speed, and the exerted force is measured by a load cell. At the flow centre of the nozzle, a desired uniaxial extensional flow is achieved. At the nozzle wall, a shear contribution is emerged and subtracted from the measured transient stress by fitting the sample fluid to a power-law behaviour based on the theory developed by Binding (1988). The HCF has previously been successfully employed to estimate extensional viscosity for materials, such as, doughs (Andersson et al. 2011; Oom et al. 2008), protein melts (Gillgren et al. 2010), mineral suspensions (Isaksson et al. 1998) and dairy products (Stading and Bohlin 2001). Furthermore, samples such as liquid medicine and different dispersions (e.g. paints) are also measurable with the HCF method. The use of a hyperbolic contraction for measuring extensional deformation has also been used for measurements on polymer melts by Baird and Huang (2006), Baird et al. (2010), Collier at al. (1998), Kim et al. (1994) and James et al. (1990). In addition, it has been utilised on the micro scale for planar extensional measurements (Campo-Deano et al. 2011; Ober et al. 2013; Oliveira et al. 2007).

An issue with converging flow is the presence of shear deformation at the tube wall, and therefore the design of the converging region is highly important in order to achieve as constant and shear-free

extensional flow as possible. Previous work on numerical simulations of viscoelastic fluids has demonstrated that the hyperbolic configuration is a suitable candidate geometry for achieving practically constant uniaxial extensional flow (Nystrom et al. 2012). In the HCF, shear contribution is minimized through the smooth contraction geometry compared to other contraction-flow alternatives i.e. vortex activity is removed.

To further improve the HCF it would be desirable to study the validation of the Power-law assumption, or to find an alternative approximation for the shear contribution and calculation of the extensional viscosity. A draw-back with using the Power-law assumption is that it is not viscoelastic, i.e. memory-effects are not included. This validation can be done through numerical simulations of the complex flow arising in the converging or contracting region in the nozzle of the HCF. Studies on viscoelastic flow through an abrupt 90^{O}-corner 4:1 contraction and 4:1:4 contraction-expansion have long been considered as a set of benchmark problems on which numerous studies are available (see review papers Walters and Webster (2003), Baaijens (1998), White et al. (1987), and the extensive work of Boger (1987) and Binding et al. (1998). The non-Newtonian fluids primarily considered are viscoelastic Boger fluids (Boger 1977) - highly elastic, dilute polymer solutions with constant shear viscosity. The transient extensional flow achieved in the contraction can give rise to a significant contribution in total pressure drop over the converging region, a contribution greater than that of shear flow. Experimental results by Nigen and Walters (2002) show an increase in pressure drop over axisymmetric contractions for viscoelastic Boger fluids compared to Newtonian fluids with the same shear viscosity. Rothstein and McKinley (1999, 2001) have shown a large increase in the so-called 'Couette correction' (excess pressure drop, *epd*) for contraction-expansion flow independent of contraction ratio and corner curvature. The *epd* extracted over the hyperbolic contraction has shown a substantial increase with rising Weissenberg numbers, when compared to an abrupt 90^{O}-corner contraction flow counterpart (Nystrom et al. 2012). Of the many factors influencing steady-flow pressure-drops, key factors affecting the increase in *epd* have been suggested to be a strong dependence on first normal stress difference (N_1) and extensional viscosity (η_e) response (see Binding 1991) and Debbaut and Crochet (1998). This has been confirmed computationally in the work of Aguayo et al. 2008, Walters et al. 2009a, 2009b, and Tamaddon-Jahromi et al. 2010, 2011. by comparing the *epd* in contraction-expansion flow for different constitutive models. A high level of extensional viscosity (η_e) has been shown to increase *epd-measure*, whilst in contrast, a strong dependence on N_1 was observed to *decrease epd*.

The present work analyses the flow through the contracting region of the HCF in order to isolate shear and elastic effects on the measured pressure drop. Currently, a test sample in the HCF is fitted to a Power-law model, for which a shear contribution can be calculated for each measurement. Thus, there is a limitation in the testing in that it can only be used for shear-thinning materials. By introducing viscoelastic properties as well, the shear contribution can be quantified numerically, whilst at the same time avoiding the Power-law fitting. One aim of the present paper is focused on comparing the outcomes from simulated and experimental *epd*-results over the hyperbolic contraction flow. An ultimate target is then to go on to utilise this knowledge to examine the potential for and limitations of using pressure drop calculation as an estimation measurement to determine extensional properties. Based on predictive findings by Tamaddon Jahromi et al. (2010, 2011), the FENE-CR model (Chilcott and Rallison 1988) has been chosen as an appropriate mathematical model to mimic well-characterised Boger fluids, while the LPTT model has been chosen

for its shear-thinning properties. The Oldroyd-B model is also used to compare and contrast incrementation in rheological properties across models and identify the corresponding influences impacting upon *epd*-estimation. The numerical results are subsequently compared with experimental findings to confirm the numerical predictions extracted, through such an axisymmetric hyperbolic contraction domain.

2. Flow and Governing Equations

The governing equation system for isothermal, viscoelastic, incompressible flow is composed of the conservation of mass and transport of momentum equations, defined as:

$$\nabla \cdot \mathbf{u} = 0, \tag{1}$$

$$\mathrm{Re}\left(\frac{\partial \mathbf{u}}{\partial t} + \mathbf{u} \cdot \nabla \mathbf{u} \right) = -\nabla p + \nabla \cdot (\boldsymbol{\tau} + 2\beta \mathbf{d}) . \tag{2}$$

Here, ***u***, ***τ***, and *p* denotes the velocity vector, the extra-stress tensor and the hydrodynamic pressure; temporal and spatial differential operator notation is implied over the space-time domain (x, t). The rate-of-deformation tensor, $\frac{\nabla \mathrm{u} + \nabla \mathrm{u}^{\mathrm{T}}}{2}$ is indicated by $\mathbf{d}$. The zero shear viscosity (η_0) of the fluid can be divided into solvent (η_s) and polymeric contributions (η_p) defining the solvent-viscosity ratio parameter as $\beta = \frac{\eta_s}{\eta_s + \eta_p}$ (β=0.9 or 0.1; see Table 1). Accordingly, the non-dimensional Re-number is defined as: $Re = \frac{\rho \mathrm{U}_{\mathrm{avg}} \ell}{\eta_s + \eta_p}$, where ρ , ℓ and U_{avg} represent fluid density, characteristic length-scale (contraction gap-width radius, $2r_1$) and characteristic velocity-scale (Q/A, average upstream velocity, determined on the base flow rate for contraction ratio 4:1, see below), respectively. A creeping flow is assumed ($Re \approx 0(10^{-2})$) and as a consequence, the momentum convection term has negligible contribution.

The numerical algorithm utilized in the present study of this hyperbolic contraction flow is that of a hybrid finite element/finite volume scheme. A thorough description of this numerical scheme can be found in Wapperom and Webster (1998, 1999), Aboubacar and Webster 2001, Webster et al. 2005, and Nystrom et al. 2012). In short, the finite element domain is discretised into parent triangular-cells consisting of six nodes, three vertex nodes and three mid-side nodes; upon this tessellation the finite volume child triangular sub-cell arrangement is constructed. The power of the hybrid scheme is that the momentum and continuity equations are approximated by the finite-element (*fe*) approach, whereas the finite volume approximation is utilised for the extra-stress constitutive equation. The time-stepping procedure consists of a two-step Lax-Wendroff method developed through a semi-implicit Taylor series expansion in time. An incremental pressure-correction methodology is utilised and divided into three stages, where the Galerkin spatial finite element (*fe*) discretisation is engaged for the momentum equation at the first stage, followed by the pressure-correction at the second stage and finally the incompressibility correction constraint is employed at the last stage. Two different solvers are employed; the element-by-element Jacobi iterative scheme for the first and last

stages, and a direct Choleski decomposition/back-substitution solver for the second pressure-increment stage.

Numerical simulations were performed on three hyperbolic contractions ratios: 4:1, 8:1 and 15:1 for various choices of constitutive models. The mesh characteristics of the two configurations are defined in Fig.1. The inlet radius (r_0) and the outlet radius (r_1) in Fig. 1a are set to 4 units and unity, respectively (setting the base relative flow rate Q=1); 8 units and unity Fig. 1b and 15 units and unity in Fig. 1c. The total length of the computational domain is fixed on 31 units, of which the contracting region length (H) is set to 15 units. The radius of the hyperbolic profile can be described by:

$$r(z) = \frac{r_0}{\sqrt{\frac{z}{H}\left(r_0^2 / r_1^2 - 1\right) + 1}} \tag{3}$$

Only half the fluid domain is depicted in Fig. 1, upon which a symmetry boundary condition is imposed at the centreline, with no-slip imposed on the wall. A constant-viscosity pressure-driven Poiseuille flow is prescribed at the inlet and a natural streamwise (open) exit condition is established at the outlet. In all cases, a pressure reference is fixed at a single location on flow-exit to remove the indeterminacy of pressure and all solutions are reported under steady-state conditions.

The *excess pressure-drop* (*epd*), is defined as the ratio between the pressure-drop for a Boger fluid to that for a corresponding Newtonian fluid (Szabo *et al.* 1997, Aguayo *et al.* 2008, and Binding *et al.* 2006):

$$epd = \frac{\left(\Delta p - \Delta p_{fd}\right)_B}{\left(\Delta p - \Delta p_{fd}\right)_N} \tag{4}$$

where $\Delta p_{fd} = \Delta p_u L_u + \Delta p_d L_d$.

This is a relative pressure drop correction of Couette-type, comparing Boger fluid (B) to Newtonian (N) Couette-estimates, which eliminates the inlet and outlet contribution to the overall pressure drop (Δp). The subscripts *fd* stands for fully-developed, *u* for upstream and *d* for downstream. L_u *and* L_d is the distance from an inlet sample-point to front-face and from front-face to exit, respectively. In this paper, fully developed conditions are taken to lie within 1% of fully-developed τ.

The respective models used in the present study are those of the Oldroyd-B model (Davies and Devlin 1993; Hinch 1993; Renardy 1995), the FENE-CR (Finitely Extensible Nonlinear Elastic-Chilcott Rallison) Chilcott and Rallison (1988) and the LPTT (Linear Phan-Thien/Tanner) (Phan-Tien and Tanner 1977; Phan-Tien 1978) model, for which their corresponding material and rheometrical functions are presented in Table 1, Table 2, and Fig. 2.

Newtonian solutions, characterised by a constant shear viscosity and a lack of elastic contribution (normal stress), are taken as base reference for the viscoelastic calculations. The constitutive equation for the FENE-CR model is expressed as follows:

$$f\left[\mathrm{Tr}(\mathbf{A})\right](\mathbf{A} - \mathrm{I}) + De\,\overset{\nabla}{\mathbf{A}} = 0 \tag{5}$$

The extensibility parameter L in the FENE-CR model is fitted to control the elongational level and is incorporated in the stretch function:

$$\mathrm{f}(\mathrm{Tr}(\mathbf{A})) = \frac{1}{1-\mathrm{Tr}(\mathbf{A})/\mathrm{L}^2} \tag{6}$$

An increasing finite extensibility parameter (*L*) results in a higher plateau level in extensional viscosity. The dimensionless Deborah number is then defined as the product of a characteristic relaxation time (*λ*) and a characteristic deformation rate ($\dot{\gamma}$), $De = \lambda\dot{\gamma}$. For an axisymmetric contraction, as used here, the characteristic deformation rate is calculated as $\dot{\gamma} = \frac{Q}{\pi \mathrm{R}_0^3}$, where Q is the volumetric flow rate and R_0 is the radius of the contraction. Hence the Deborah number can be expressed as $De^{\mathrm{num}} = \frac{\mathrm{U}_{\mathrm{avg}}}{\ell}$. ***I*** is the identity tensor, ***A*** the stress conformation tensor and Tr is the trace operator ($Tr(\mathbf{A}) = A_{11} + A_{22} + A_{33}$). The stress (**τ**) can thus be expressed as:

$$\boldsymbol{\tau} = \frac{(1-\beta)}{De} f\left[Tr(\mathbf{A})\right](\mathbf{A}-\mathbf{I}). \tag{7}$$

The second model used in this study is that of the LPTT model, which predicts a decreasing shear viscosity with increasing shear-rate and has a controllable extensibility parameter. N_1 is weaker than in the FENE-CR model (see Fig. 2c). The constitutive equation for the LPTT-model has the following expression:

$$f(\boldsymbol{\tau})\boldsymbol{\tau} + De\overset{\nabla}{\boldsymbol{\tau}} = 2(1-\beta)\mathbf{d}, \tag{8}$$

where $\mathbf{d}$ represents the rate of deformation and the upper-convected material derivative of stress, $\overset{\nabla}{\boldsymbol{\tau}}$ and $f(\boldsymbol{\tau})$ are defined as:

$$f(\boldsymbol{\tau}) = 1 + \frac{\varepsilon_{\mathrm{PTT}}}{(1-\beta)}\mathrm{tr}(\tau) \tag{9}$$

The non-dimensional model parameters selected for investigation are $\varepsilon_{\mathrm{PTT}}$=0.05, $\varepsilon_{\mathrm{PTT}}$=0.042 and $\varepsilon_{\mathrm{PTT}}$=0.01. Here, $\varepsilon_{\mathrm{PTT}}$=0.05 is chosen to match the extensional viscosity plateau of FENE-CR, L=3 model, $\varepsilon_{\mathrm{PTT}}$=0.042 is chosen to match the extensional viscosity plateau of FENE-CR, L=5 model and $\varepsilon_{\mathrm{PTT}}$=0.01 is chosen to match the extensional viscosity plateau of FENE-CR, L=10 model. As demonstrated in Fig. 2, the properties in N_1 for these three LPTT models are essentially the same; whilst, viscometric response for $\varepsilon_{\mathrm{PTT}}$=0.05 expresses a lower limiting η_e-cap than that for $\varepsilon_{\mathrm{PTT}}$=0.042. By direct inspection between the material functions of the LPTT model and the FENE-CR model, shear-thinning effects may be isolated. The Oldroyd-B model on the other hand, is a constant shear viscosity fluid that displays extreme strain-hardening already at an extension rate of $\dot{\varepsilon} = 0.5$ (see Fig. 2). The Oldroyd-B model is recovered as the limiting case (*f*=1). In addition, in Fig. 2c, the experimentally-measured stress-data (N_1) are superimposed against those predicted in theory by the

FENE-CR model. Here, experimental N_1 matches best, in a least-squares best-fit sense, against the FENE-CR(L=5) theoretical data, providing an intercept at rates of $O(10^2)$. Otherwise, the experimental data straddles the theoretical data curves from (L=3), to (L=5), to (L=10).

3. Experimental section

3.1 Materials

Two types of model fluids are used for the method evaluation, differing in viscoelastic properties; a Newtonian fluid, and a Boger fluid. The fluids under consideration in this experimental section are based on a solution of glucose syrup dissolved with water and polyacrylamide (PAA). To control the level of viscosity, the syrup was diluted with a desired amount of distilled water. Boger fluids are model fluids with a constant shear viscosity and are highly elastic at room temperature. The characteristics of the test fluids are given in Table 3. The light syrup used in the present study was provided from Dan Sukker (Danisco Sugar, Oslo) and the polyacrylamide (92560-10G PAA, Mw=5-6 MDa) was provided from Sigma-Aldrich Co., USA. The samples were all left on a magnetic stirrer overnight at low speed to ensure satisfactory homogeneity. The PAA was first dissolved, in distilled water for 24 hours, with a magnetic stirrer at room temperature before being added to the syrup. The test fluids were characterised at a constant temperature of 20°C, controlled with a water jacket, and the rheological properties were determined with a controlled strain device (TA Instruments, Model: ARES-G2, USA) with a cone-plate system (40 mm in diameter, cone angle of 0.398 rad). The truncation gap was 0.0482 mm. Both dynamic oscillatory and steady shear flow testing was performed to determine the dynamic viscosity $\eta^*(\omega)$, shear viscosity $\eta(\dot{\gamma})$ and the first normal stress coefficient $\Psi_1(\dot{\gamma})$. The exposed edges were covered with paraffin oil to reduce water loss from the sample during performance of the measurements.

3.2 Experimental measuring technique

Here, an experimental setup has been used to measure uniaxial extensional flow, based on a hyperbolic contraction flow device, described by Wikström and Bohlin (1999) mounted on an Instron Universal Testing Machine model 5542 (Instron Corporation, Canton, USA) with a measuring range of 500 N and accuracy of 1.2-N (Stading and Bohlin 2000). The fluid is contained in a temperature controlled cylinder (82 mm long) and pressed by a piston at constant speed (0.5 mm/minute – 15 mm/min) through an axisymmetric hyperbolic contraction nozzle. The nozzle is designed to give a constant extension rate and is mounted directly in contact with the load cell of the instrument to minimize the influence of friction. A schematic drawing of the hyperbolic contraction flow device is shown in Fig. 3. Various contraction ratios can be obtained by switching the particular choice of nozzle. At the start of the measurements the sample goes through a stress growth period before reaching a steady state. The contraction nozzle rests on a load cell and the exerted force on the load cell is measured. After passing the contraction nozzle the test sample is let to flow out to room conditions. The force needed to push the sample through the nozzle is estimated to correspond to a pressure drop, from which extensional properties of the test sample can be determined.

The sample fluid was completely filled into the sample tube with the attached contraction nozzle and allowed to rest for at least 5 minutes before the start of the measurement to attain a relaxed sample. The temperature was kept constant at T=20°C by a temperature jacket, which was coupled to a controlled circulator Julabo Model FP40 (Julabo Labortechnik, Seelbach, Germany). The

measurements were performed at different strain-rates at piston rates ranging from 0.5 mm/s to 15 mm/s and reproduced three times to check reproducibility. The samples were tested for a contraction ratio of 15:1 and 10:2.15. The total Hencky strain experienced by a fluid element, calculated as: $\varepsilon_H = \ln\left(\frac{r_0}{r_1}\right)$ is presented in Table 4, together with the dimensions of the contraction geometry. This is the same range as is often obtained in the CaBER measurements.

The Deborah number (*De*), defined in the modeling section above as $De^{\exp} = \lambda_R \frac{Q}{\pi R_0^3} = \lambda_R \frac{\nu}{R}$, is calculated for all the measurements at different flow rates. ν denotes the flow velocity and R is the radius of the outlet. The relaxation time of the fluid in extensional flow was determined with a capillary break-up extensional rheometer (Haake CaBER, Thermo Scientific).The measurement was performed at T=23° with a plate diameter of 6 mm. Moreover, the initial and final height was set to h_i=1.99 mm h_f=8.55 mm, obtaining a final aspect ratio of A_i=1.43

4. Results and discussion

4.1 Numerical results

4.1.1 Influence of contraction ratios

Three different axisymmetric hyperbolic contraction ratios were studied numerically in order to examine the effect of contraction ratio on fluid flow and pressure drop. Firstly, the *onset of vortex development* in the hyperbolical flow was studied through streamline patterns under identical flow rate for the three contraction ratios studied. The result can be seen in Fig. 4. , where streamline contours are plotted in core flow at equal increments of 0.05, covering contour levels $0 \le \psi \le 0.45$ for the FENE-CR, *L*=5 model. The stream function was calculated for the *De*-range of 0.1-100 but only results for *De*=0.1 and *De*=5 are shown. In the case of vortex development, the ψ –peak value is specified. Vortex development is prominent only for the 15:1 contraction ratio (see Fig. 4. e-h). This is due to the *sharper corner* attained in the 15:1 contraction. Furthermore, some vortex enhancement is observed over increasing De-numbers, where the diameter of the vortex is increased by 1.7 units going from *De*=0.1 to *De*=5.0. A small indication of vortex development can also be observed in the 8:1 contraction ratio (Fig. 4. c-d), although the peak value is practically zero. The peak value is also zero in Fig. 4. g-h where a rounded-corner is introduced to the 15:1 contraction ratio; the development of the vortex is delayed and the size of the vortex is decreased to some extent in agreement with the work of Rothstein and McKinley (2001). Compared to a sharp contraction having ψ –peak values above 0.5 for *De*>1, the peak values detected here are considerable smaller. No vortex can be detected in the 4:1 contraction ratio for the whole De-number range tested. These results are important to take into account during experimental measurement, especially when using the 15:1 contraction, giving slightly lower values due to the vortex presence lowering the actual contraction angle. In this respect, constructing a 15:1 contraction ratio nozzle with a rounded-corner may prove beneficial. Note that, vortex development is also fluid and rate dependent, influencing the tendency to develop vortices (and that vortex presence itself may be undesirable depending upon the processing conditions themselves).

Secondly, the radial stress (τ_{rr}) (principal component of second-normal stress-difference) and axial stress (τ_{zz}) (principal component of first-normal stress-difference) were studied also through contour plots in for the same flow rate (for the non-dimensional flow rate of Q=1 units) on all contraction ratios. Consistently, the radial stress reaches its maximum value at the boundary wall beyond the contraction, while the axial stress increases towards the contraction exit. It is interesting to note that the axial stress is dominant here with a radial stress close to zero, implying that the influence of shear stress is minimized. Additionally, one can see the axial stress (τ_{rr}) increasing towards the wall with a maximum of 2.32 at r=1 in Fig. 6. From the contour plots in Fig. 5, it can also be observed that the contraction ratio seems to have little significant influence on stress levels. The reason for the larger variation in normal stress between the contractions ratios is more likely to be caused by exit effects. From the radial and axial normal stresses, the first normal stress difference can be calculated ($\boldsymbol{N}_1 = \boldsymbol{\tau}_{zz} - \boldsymbol{\tau}_{rr}$) and N_1 line plots are displayed in Fig. 7 together with rates and extensional viscosities in both extension Fig. 7A and in shear Fig. 7B. The results are compared both on changing contraction ratio, whilst keeping the flow rate constant (*Q=1* units), and increasing flow rates (the maximum inlet velocity is set constant (U_{max}*=0.125* units) for all contraction ratios). Since the axial stress is the dominant factor at the symmetry line, N_1 will be a function of $\boldsymbol{\tau}_{zz}$, which is reflected in Fig. 7 through a positive N_1 reaching a plateau after the start of the contraction in extension. An increase in N_1 can be seen with increasing *De*-number and the onset of N_1–rise is shifted closer to the start of the contraction with rising *De*-number. The increase in the normal-stress component, as the contraction plane is approached, is related to the increase in pressure drop, similarly to that experienced in velocity gradient. At fixed flow rate and as analogous to the radial and normal stresses, N_1 shows no variation dependence on contraction ratio (see Fig. 7A a). In contrast, *an increase in flow rate* going from 4:1 to 15:1 contraction ratio results in a 8.6 unit increase in such stresses in Fig. 7A b), which can also be observed for N_1 in shear (Fig. 7B a,b).

Furthermore, the comparison of numerical prediction to theoretical rheometric functions on N_1 is provided in Fig.8, for increasing localized rates (strain and shear) at fixed flow rate. These data show close agreement in shear (Fig.8b), throughout the range $0.2 < \dot{\gamma} < 3$ and for all three contraction ratios. The agreement established in extension (Fig.8a) holds over the earlier rate range of $0.002 < \dot{\varepsilon} < 0.009$. In a, a steeper slope is observed for the calculated numerical N_1 *prediction in extension* for the different contraction ratios to the corresponding theoretical value; but there is close agreement between the data for 8:1 and 4:1 contraction ratios. The discrepancy between the prediction (inhomogeneous) and theory (homogeneous) is in the range of 9 % at low De and 6 % at high De. Hence, it is to be expected that extensional viscosity will be over-predicted for higher rates and under-predicted for lower rates. In contrast studying N_1 *in shear* (b), closer agreement is established between numerical predictions (inhomogeneous) and corresponding theoretical values (homogeneous) as higher rates are approached.

Thirdly, the shear rate along the boundary wall and strain rate along the symmetry line are plotted in Fig. 7c-d. The shear and strain rate are extracted from the numerical calculations through two invariants of the rate of deformation tensor, $\mathbf{d}$ (Debbaut and Crochet 1988). These are denoted as:

Shear-rate: $\dot{\gamma} = 2\sqrt{\mathrm{II}_{\mathbf{d}}}$ (10)

Strain-rate: $\dot{\varepsilon} = 3\frac{\mathrm{III_d}}{\mathrm{II_d}}$ (11)

where, $II_{\mathbf{d}}$ and $III_{\mathbf{d}}$ are the second and third non-zero invariants of the rate of strain tensor d_{ik}. For uniaxial extensional flow the invariant $\dot{\varepsilon}$ reduces to the usual extensional strain-rate. Analogously, the invariant $\dot{\gamma}$ reduces to the usual shear-rate in steady simple shear flow:

$$\mathrm{II_d} = \frac{1}{2}\mathrm{tr}(\mathbf{d}^2), \qquad \mathrm{III_d} = \det(\mathbf{d}). \tag{12}$$

Analogous to results for N_1, neither the shear or strain rate seem to be significantly affected by the increase in contraction ratio as shown in Fig. 7A(a,c) and Fig. 7B(a,c). Naturally, a major increase can be seen in Fig. 7A(b, d) and in Fig. 7B(b, d) both shear and strain rate when *increasing the flow rate* going from 4:1 to 15:1 contraction ratio. The shear rate reached at the exit is prominent, and larger than that reached in strain rate. In Fig. 7A(e,f) the extensional viscosity is in the same range for all contraction ratios when the flow rate is kept constant, increasing by a tenfold towards the exit. However, this increase is negligible when introducing increasing flow rate which has a high impact on the extensional viscosity attained. Here, a nearly constant extensional viscosity is reached sooner, the higher the contraction rate (z≈5 for 15:1 and z≈7 for 8:1 contraction ratio).

Finally, the *epd* (*excess pressure drop* defined above) is calculated and compared for three constitutive models in Fig. 9. Here, the *flow rate was fixed* for all contraction ratios. In contrast to the previous results, a clear influence of contraction ratio on *epd* can be detected for all constitutive models considered. There is an overall rise in *epd* for increasing deformation rate (*De*) in the low *De*-range. In Fig. 9a, the *epd* for the Oldroyd-B model is shown (note, at an expanded *De*–scale), where the largest *De*-number reached was 15 (constrained by lack of finite-extensibility). For larger De-numbers (De>15) either oscillation or divergence is encountered and no reliable results can be extracted. A smaller difference in *epd* can be seen between the 8:1 and 15:1 contraction (7% increase) options, than between the 4:1 and 15:1 contraction (50% increase).

The FENE-CR model results are plotted in Fig. 9b, where there is initial *epd*-rise observed up to *De*~15, followed by a gradual tail-off to a limiting plateau level in the high *De*-range. The counterpart data for the shear-thinning LPTT model is provided in Fig. 9c, which displays a similar initial *epd*-rise, but now observed only up to *De*~2, where there is a pronounced overshoot, before proceeding to decline and again, gradually tail-off to a limiting plateau level in the high *De*-range. In contrast to the FENE-CR results, this overshoot and fall with LPTT may be attributed to its additional shear-thinning property. Moreover, Oldroyd-B findings in the restricted low deformation-rate range (De≤2), are consistent with both those for FENE-CR and LPTT, bar the exaggerated low trend in *epd* noted with the 4:1 geometry. This is somewhat to be expected, as the differences in rheological properties between Oldroyd-B and FENE-CR within such a low deformation-rate range, are much closer. As expected, a higher level of *epd* is achieved for the larger contraction ratio for each model taken in turn. This is deemed to be due to the elevated deformation rates (and stress) generated in the larger contraction ratio instances. In addition, the *epd*-values for different sample points along the x-axis were compared and no significant change (0.2%) in *epd* was detected. On the contrary, the exit-correction seems to have a major impact on the pressure drop. In this work, the exit condition is set to have zero reference pressure at the exit flow station in order to maintain fully-developed shear

flow conditions at the exit. In future work, it is intended to also test an alternative exit condition and to examine its influence; for example, to replace with a die-swell exit condition.

4.1.2 Influence of rheology

In order to segregate the shear and N_1 effects, using the base-case 4:1 hyperbolic contraction configuration, a comparison across constitutive model solutions was performed. Under such a comparison the model parameters are adjusted and various competing factors on *epd* are analysed. The results from the constitutive model comparison are depicted in Fig. 10. The effect of elevating extensional viscosity (η_e) is studied through the increase of the *L*-parameter in the FENE-CR model, see Fig. 10a. The strong elevating effect on *epd* of increasing η_e is apparent in Fig.10a. For *De*>2, a strengthening of N_1 can also be observed with rising L-parameter, see Fig.10c. However, the strengthening of N_1 is not as pronounced as the strengthening of η_e.

Next, the ε-parameter in the LPTT-model was varied from ε=0.01, to ε =0.042 and ε=0.05. As can be seen in Fig. 2, the extensional viscosity of the different ε-parameter levels in the LPTT model are matched to the different L-parameters in the FENE-CR model. However, there is a weakening in N_1 in the LPTT-model compared to the FENE-CR model and there is a shear-thinning effect introduced into the LPTT-model. The level of shear-thinning remains practically unaltered for ε=0.042 and ε=0.05, while for ε=0.01 the shear-thinning effect is reduced. The onset of shear-thinning is also somewhat delayed to a De=1 for the ε=0.01. From the findings in Fig. 10b, a decrease in *epd*-level is observed for increasing ε. Comparing ε=0.01 to ε=0.05 and ε=0.042, the decrease in *epd* can be explained through decreasing the limiting plateau level of extensional viscosity (η_e), weakening in N_1 and increasing shear-thinning behaviour. Overall, an initial rise can be observed, followed by a monotonic decline for increasing *De*-numbers. Since η_e has reached a plateau at around *De*~30 for all parameters tested, the decline must be due to the decline in shear-viscosity with increasing *De*. The onset of shear-thinning is delayed for ε=0.01 compared to ε=0.042 and 0.05, reflected in the epd-result with a delayed epd decline for ε=0.01. Decreasing ε=0.05 to ε=0.042 results in a slightly lower *epd*-value. Here, the decrease in *epd* is due to η_e and N_1 weakening. Thus, the level of shear-thinning has a larger effect on *epd*-levels, when compared to the influence of η_e level.

Lastly, the models are compared in Fig. 10c. In addition to the FENE-CR and LPTT model, results for the Oldroyd-B model are also included. For the Oldroyd-B model the N_1-dependence is quadratic with unbounded growth in extensional viscosity at a finite deformation-rate. This behaviour is reflected in the *epd*-results with a steep *epd*-increase for increasing *De*-numbers, confirming the elevating effect of η_e and a strong N_1-dependance. Since the η_e level is matched between the FENE-CR, L=5 and the LPTT model ε=0.042, the contra effect on the level of epd reached for the LPTT-model may be attributed to shear-thinning effects (and so to N_1 weakening also). Moreover, the level of epd reached for both these models is the same for *De*<1, that is before the onset of shear-thinning. Thus, corresponding to the findings in Fig. 10b, the decline in epd may be unambiguously attributed to shear-thinning effects. These results are confirmed by the results presented by Tamaddon-Jahromi et al. (2011), showing a lowering of epd with η_e damping and an elevation due to N_1 damping. Furthermore, the reduction in LPTT *epd*-data is shown to be primarily due to shear-thinning effects. In conclusion it can therefore be assumed that there is a presence of shear effects in the HCF device, which should be taken into account during experimental measurement.

Next, N_1 along the symmetry line and along the boundary wall is studied in Fig. 10d and Fig. 10e, respectively for *De*=5. Since the N_1-dependence is the strongest for the Oldroyd-B model, the largest N_1 is reached for the Oldroyd-B model. In Fig. 10d larger N_1 is reached for the LPTT model along the symmetry line in contrast to the boundary wall, where larger N_1 is attributed to the FENE-CR result.

4.1.3 Influence of fluid - Adjustment of solvent-fraction β

Effect of fluid composition can also be studied through the variation of solvent fraction (β), and its impact on pressure drop at fixed flow rate. Here, the results for two different solvent fractions, β=0.9 (high solvent contribution, as with typical Boger fluids) and β=1/9 (high polymeric contribution) are presented in Fig. 11, where also a comparison between different models is performed (with a zoom for low rates). For all three models tested, a lower β-factor (increase in polymeric content) produces considerably steeper *epd*-rise. The critical *De*-number reached for β=1/9 was De_{crit}=1 for the Oldroyd-B model; De_{crit}=3 for the FENE-CR model; and De_{crit}=2 for the LPTT model. With β=1/9 and over such a restricted deformation-rate range, the three model *epd*-solutions are comparable, reflecting common low deformation-rate rheology. Considering the adjustment in solvent fraction from β=1/9 to β=0.9, firstly one notes the consistent decline in *epd*-level in all three models, associated with the order of magnitude reduction in polymeric component stress levels. Secondly, whilst focusing on the *epd*-data(β=0.9) and *De*≤50, one identifies the deviation, form and curve-intercepts apparent in the results. The deviation between the FENE-CR and the LPTT *epd*-data(β=0.9) is now enlarged from the (β=1/9)-status, onset at *De*~2 and sustained by *De*~10. Here, decreasing polymeric contribution from β=1/9 to β=0.9, has lessened the impact of shear-thinning; so greater departure between the FENE-CR and LPTT *epd*-data(β=0.9) at these larger rates must be associated with their increased disparity in N_1-weakening (extensional effects are matched). In contrast, the Oldroyd-B *epd*(β=0.9) result is also revealing. Its sharp *epd*-rise for *De*≥15 (divergence above *De*=18), may be strictly inferred from the FENE-CR result and intercept, to be associated with its unbounded extensional viscosity response (extensional stress effect). Tracing backwards in decreasing *De*, the intercepts between the Oldroyd-B *epd*(β=0.9)-curve, and first that for FENE-CR(*De*~11), and subsequently for LPTT(*De*~9), indicate in each case the precise switch-over stage at which *epd* is dominated by extensional stress influence, as opposed to stress from shear deformation.

4.2 Experimental results

Experimental results were performed on the hyperbolic contraction flow device (HCF) in order to evaluate the numerical predictions. Two different model fluids, a Newtonian and a Boger, were developed and the characteristics of these fluids are summarized in Table 5. Measurement of a Newtonian fluid through the hyperbolic contraction flow was performed to serve as a baseline for comparison of the non-Newtonian test fluids. In Fig. 12 the rheological properties from shear viscosity measurements for the model fluids are represented. As can be observed, the shear and dynamic viscosity of the Boger fluid are almost constant over several decades of shear-rate and at the same level as the Newtonian fluid. From determination of the first normal stress coefficient, one can observe that the Boger fluid is elastic, unlike the Newtonian fluid, which shows little normal stress development. Since the viscosities of the Newtonian and Boger fluids are set at the same level, the elastic effects of the Boger fluid can be isolated. The elastic properties were studied through measurements in the HCF device of both fluids and findings are presented in Fig. 13 and Fig. 14. Measurements were performed on two different contraction ratios: 15:1 and 10:2.15 (≈4:1). However, due to the low shear viscosity of the Boger fluid, the measured load with the 4:1 nozzle

was too low to be differentiated from the background noise detected. In Fig. 13 pressure drops for increasing flow rates are reported at ambient temperature of T=20^{O}C. Taking error-bars into account, the steepest slope can be observed for the Boger fluid, initially linear and at higher rates, with ascending deviation from the linear relationship. As anticipated, the Newtonian pressure drop is linearly proportional to the volumetric flow rate, and here, close agreement is established between experimental measured values and those numerically predicted; for the Boger fluid, with more dramatic larger pressure drops recorded, the position is somewhat similar, noting the error-bar indication on the experimental reading at the largest flow rate taken. For comparison extensional measurement were also performed with a capillary break-up extensional rheometer (*CaBER*). The maximum Hencky strain attained was 1.46 and the relaxation time of the Boger fluid was determined to be 1.40 s.

In Fig. 14 the dimensionless excess pressure drop for increasing *De*-numbers are reported for the Boger fluid measurement through the 15:1 contraction ratio. The dimensionless pressure drop from the experiments are calculated by dividing the measured pressure drop of the Boger (ΔP_B) with the results of the Newtonian fluid (ΔP_N) at any given flow rate; thus the pressure drop will be a measure of the elasticity. In the absence of elasticity (*De*->0) this pressure drop measure should tend to unity, and the more elastic the Boger fluid, the higher the dimensionless pressure drop. Gathered from Fig. 14, the Boger fluid pressure drop is observed to lie well above the Newtonian reference line, indicating that the HCF is able to detect the elastic contribution of the Boger fluid. Furthermore, the pressure drop approaches unity for *De*->0. *De*=7 was the highest Deborah number attained in the experiments due to the practical limitation in measurement with the load cell. Numerical predictions with the FENE-CR model are also included in Fig. 14 with varying *L*-parameter. This comparison clearly indicates strong correlation between the predictions, with *L*=3 and L=5 settings, and the Boger experimental results, providing a tight window of capture of the experimental pressure drop data. In particular, one notes the close agreement at larger flow-rates equivalent to *De*>4, against the L=5 setting. Overall, such findings demonstrate that the hyperbolic contraction flow is well capable of detecting elastic properties of the fluid and that numerical simulations are indeed able to evaluate the flow response of such test fluids (Stading and Bohlin 2000, 2001). Beneficially, the hyperbolical contraction flow technique is straightforward and simple to perform - the Hencky strain can be set by changing contraction ratio, non-homogenous fluids can be tested, and one can directly determine the degree of elastic behaviour of the fluid. However, the lower the fluid shear-viscosity, the harder it becomes to extract accurate data, and where fluctuations of the measured loads may be encountered. As a consequence, the current measuring range for the pressure drop is limited to that equivalent for the load cell.

5. Conclusion

In this study, the hyperbolic contraction flow method (HCF) has been evaluated by means of both numerical prediction and experimental measurements. Numerical solutions have been analysed for steady-state, viscoelastic flow through three different hyperbolic nozzles with different contraction ratios. Through various choices of constitutive model, the influence of shear and normal stress differences on such flows has been studied. The numerical results have also been compared to experimental measurements on corresponding model fluids at the highest contraction ratio. On correcting the measured pressure drop, by subtraction of the exit and entry pressure drop

contributions (excess pressure drop), a more realistic measure of the elastic properties has been achieved. The numerical predictions are shown to reflect the complex flow in the contraction and predict the increase in pressure drop with increasing deformation rate. The predictions show an influence of shear on the pressure drop, but it is still relatively small. Similar trends have been shown between the numerical predictions and experimental results, but the increase in predicted pressure drop was not as strong as detected within the experiments.

The numerical results presented in this paper show a minor influence of shear in the flow through the hyperbolical nozzle. Still, analysing the pressure drop over the contraction nozzle for the LPTT-model, a decline in pressure drop is observed through the hyperbolic contraction, which indicates an influence of shear in the flow. By increasing the contraction ratio, a higher extensional deformation was achieved, but also a higher influence of shear, revealing vortex formation for the highest contraction ratio. Vortex formations tend to lower the level of excess pressure drop (*epd*). This decline is, however, not as pronounced as in an abrupt 90^{O}-corner contraction; nevertheless, it should be taken into account and compensated for during measurement.

The numerical predictions were compared to experimental data for a Boger and a shear-thinning model fluid through the 15:1 contraction. Compared to the Newtonian model fluid findings, the elastic Boger fluid showed a clear increase in pressure drop, confirming that the measuring system can indeed effectively detect the extensional properties for such a test fluid. Moreover, this finding lies in close agreement with the numerical predictions, which provide a tight window of capture of the Boger experimental pressure drop data. This result has demonstrated that the hyperbolic contraction flow is indeed able to detect such elastic fluid properties, and that numerical predictions are well able to evaluate the flow response of the test fluids, as required. Moreover, the hyperbolical contraction flow technique is straightforward and simple to perform - the Hencky strain can be set by changing contraction ratio, non-homogenous fluids can be tested and one can directly determine the degree of elastic behaviour of the fluid. For the shear-thinning fluid, which lies in contrast to the *constant-viscosity* Boger fluid, a decline in pressure drop could also be observed. This decline indicates a counteracting suppressive and negative influence of shear-thinning on the pressure drop, which again, is in agreement with numerical predictions As such, these numerical predictions can thus be utilized to calculate a correction for shear. The predictions have also shown that the Binding/Bohlin correction for shear influence is a reasonably good approximation for highly shear-thinning fluids, but inadequate for fluids without strong shear-thinning behaviour.

Other major findings from this work may be summarised concisely as follows:

(i) A higher level of *epd* is achieved in larger contraction ratio instances, due to elevation in deformation rate.

(ii) It is apparent that increasing η_e has a strong elevating effect on *epd*. Yet, the level of shear-thinning has a larger effect on *epd*-levels, when compared to the influence of η_e level.

(iii) With all three constitutive models tested (Oldroyd-B , FENE-CR and LPTT), a lower solvent fraction (β-factor, increase in polymeric content) produces considerably steeper *epd*-rise. As such, consistent decline in *epd*-level is observed with adjustment in solvent fraction from β=1/9 to β=0.9.

(iv) The intercepts between the Oldroyd-B *epd*(β=0.9)-curve, and first that for FENE-CR(*De*~11), and subsequently for LPTT(*De*~9), indicate in each case, respectively, the precise switch-over stage at which *epd* is dominated by extensional normal-stress influence, as opposed to that from shear normal-stress influence.

References

Aboubacar M, Webster MF (2001) A Cell-Vertex Finite Volume/Element Method on Triangles for Abrupt Contraction Viscoelastic Flows, J. Non-Newton. Fluid Mech. 98 (2-3) 83-106

Aguayo JP, Tamaddon-Jahromi HR, Webster MF (2008) Excess Pressure-Drop Estimation in Contraction and Expansion Flows for Constant Shear-Viscosity, Extension Strain-Hardening Fluids, J. Non-Newton. Fluid Mech. 153 (2-3) 157-176

Andersson H, Öhgren C, Johansson D, Kniola M, Stading M (2011) Extensional Flow, Viscoelasticity and Baking Performance of Gluten-Free Zein-Starch Dough Supplemented with Hydrocolloids, Food Hydrocolloids (0268-005X). Vol. 25, 1587-1595

Baaijens FPT, (1998) Mixed Finite Element Methods for Viscoelastic Flow Analysis: A Review, J. Non-Newton. Fluid Mech. 79 (2-3) 361-385

Baird DG Huang J (2006) Elongational Viscosity Measurements Using a Semi-Hyperbolic Die, Appl. Rheol. 16 (6) 312-320

Baird DG, Tung WC, McGrady C, Mazahir SM (2010) Evaluation of the Use of a Semi-Hyperbolic Die for Measuring Elongational Viscosity of Polymer Melts, Appl. Rheol. 20 34900-1 - 34900-12

Binding DM (1988) An Approximate Analysis for Contraction and Converging Flows, J. Non-Newton. Fluid Mech., 27 (2) 173-189

Binding DM, (1991) Further Considerations of Axisymmetric Contraction Flows, J. Non-Newton. Fluid Mech. 41 27-42

Binding DM, Couch MA, Walters K (1998) The Pressure Dependence of the Shear and Elongational Properties of Polymer Melts, J. Non-Newton. Fluid Mech. 79 (2-3) 137-155

Binding DM, Phillips PM, Phillips TN (2006) Contraction-Expansion Flows: The Pressure Drop and Related Issues, J. Non-Newton. Fluid Mech. 137 (1-3) 31-38

Boger DV (1987) Viscoelastic Flows through Contractions, Annu. Rev. Fluid Mech. 19 157-182

Boger DV (1977) A Highly Elastic Constant-Viscosity Fluid, J. Non-Newton. Fluid Mech. 3 (1) 87-91

Campo-Deano L, Galindo-Rosales FJ, Pinho FT, Alves MA, Oliveira MSN (2011) Flow of Low Viscosity Boger Fluids through a Microfluidic Hyperbolic Contraction, J. Non-Newton. Fluid Mech., 166 (21-22) 1286-1296

Chen JS, Lolivret L (2011)The Determining Role of Bolus Rheology in Triggering a Swallowing, Food Hydrocolloids, 25 (3) 325-332

Chilcott MD, Rallison JM (1988) Creeping Flow of Dilute Polymer Solutions Past Cylinders and Spheres, J. Non-Newton. Fluid Mech. 29 381-432

Collier JR, Romanoschi O, Petrovan S (1998) Elongational Rheology of Polymer Melts and Solutions, J. Appl. Polym. Sci. 69 (12) 2357-2367

Debbaut B, Crochet MJ (1988) Extensional Effects in Complex Flows, J. Non-Newton. Fluid Mech., 30 (2-3) 169-184

Davies AR, Devlin J (1993) On Corner Flows of Oldroyd-B Fluids, J. Non-Newton. Fluid Mech. 50 (2-3) 173-191

Dobraszczyk BJ, Morgenstern M (2003) Rheology and the Breadmaking Process, Journal of Cereal Science 38 (3) 229-245

Entov VM, Hinch EJ (1997) Effect of a Spectrum of Relaxation Times on the Capillary Thinning of a Filament of Elastic Liquid, J. Non-Newton. Fluid Mech. 72 (1) 31-53

Fuller GG, Cathey CA, Hubbard B Zebrowski BE (1985) Extensional Viscosity Measurements for Low-Viscosity Fluids, J. Rheol. 31 235-249

Gupta RK (2000) Polymer and Composite Rheology. Second edition ed. Morgantown: Marcel Dekker, Inc

Gillgren T, Alven T, Stading M (2010) Impact of Melt Rheology on Zein Foam Properties, J. Mater. Sci., 45 (21) 5762-5768

Hinch EJ (1993) The Flow of an Oldroyd Fluid around a Sharp Corner, J. Non-Newton. Fluid Mech. 50 (2-3) 161-171

Isaksson P, Rigdahl M, Flink P, Forsberg S (1998) Aspects of the Elongational Flow Behavior of Coating Colors, J Pulp Pap Sci, 24 (7) 204-209

James DF, Chandler GM, Armour SJ (1990) A Converging Channel Rheometer for the Measurement of Extensional Viscosity, J. Non-Newton. Fluid Mech., 35 (2-3) 421-443

Kim HC, Pendse A, Collier JR (1994) Polymer Melt Lubricated Elongational Flow, Journal of Rheology, 38 (4) 831-845

Koliandris AL, Rondeau E, Hewson L, Hort J, Taylor AJ, Cooper-White J Wolf B (2011) Food Grade Boger Fluids for Sensory Studies, Applied Rheology 21 (1)

Meissner J (1972) Development of a Universal Extensional Rheometer for the Uniaxial Extension of Polymer Melts, Trans. Soc. Rheol. 16 405-420

Meissner J, Hostettler J (1994) A New Elongational Rheometer for Polymer Melts and Other Highly Viscoelastic Liquids, Rheol. Acta. 33 (1) 1-21

Nigen S, Walters K Viscoelastic (2002) Contraction Flows: Comparison of Axisymmetric and Planar Configurations, J. Non-Newton. Fluid Mech., 102 (2) 343-359

Nystrom M, Tamaddon Jahromi HR, Stading M, Webster MF (2012) Numerical Simulations of Boger Fluids through Different Contraction Configurations for the Development of a Measuring System for Extensional Viscosity, Rheol. Acta, 51 (8) 713-727

Ober TJ, Haward SJ, Pipe CJ, Soulages J, McKinley GH (2013) Microfluidic Extensional Rheometry Using a Hyperbolic Contraction Geometry, Rheol. Acta, 52 (6) 529-546

Oliveira MSN, Alves MA, Pinho FT, McKinley GH (2007) Viscous Flow through Microfabricated Hyperbolic Contractions, Experiments in Fluids, 43 (2-3) 437-451

Oom A, Pettersson A, Taylor JRN, Stading M (2008) Rheological Properties of Kafirin and Zein Prolamins, Journal of Cereal Science, 47 (1) 109-116

Phan-Tien N, Tanner RI (1977) A New Constitutive Equation Derived from Network Theory, J. Non-Newt. Fluid Mech. 2 353-365

Phan-Tien N (1978) A Nonlinear Network Viscoelastic Model, J. Rheol. 22 (3) 259-283

Renardy M (1995) A Matched Solution for Corner Flow of the Upper Convected Maxwell Fluid, J. Non-Newton. Fluid Mech. 58 (1) 83-89

Rothstein JP, McKinley GH (1999) Extensional Flow of a Polystyrene Boger Fluid through a 4 : 1 : 4 Axisymmetric Contraction-Expansion, J. Non-Newton. Fluid Mech., 86 (1-2) 61-88

Rothstein JP, McKinley GH (2001) The Axisymmetric Contraction-Expansion: The Role of Extensional Rheology on Vortex Growth Dynamics and the Enhanced Pressure Drop, J. Non-Newton. Fluid Mech., 98 (1) 33-63

Sridhar T, Tirtaatmadja V, Nguyen DA, Gupta RK (1991) Measurement of Extensional Viscosity of Polymer-Solutions, J. Non-Newton. Fluid Mech. 40 (3) 271-280

Stading M, Bohlin L (2000) Measurements of Extensional Flow Properties of Semi-Solid Foods in Contraction Flow, Proceedings of the 2nd International Symposium on Food Rheology and Structure, 2 117-120

Stading M, Bohlin L (2001) Contraction Flow Measurements of Extensional Properties, Transactions of the Nordic Rheology Scociety, 8-9 147-150

Szabo P, Rallison JM, Hinch EJ (1997) Start-up of Flow of a Fene-Fluid through a 4:1:4 Constriction in a Tube, J. Non-Newton. Fluid Mech. 72 (1) 73-86

Tamaddon-Jahromi HR, Walters K, Webster MF (2010) Predicting Numerically the Large Increases in Extra Pressure Drop When Boger Fluids Flow through Axisymmetric Contractions, Natural Science, 2 (1) 1-11

Tamaddon-Jahromi HR, Webster MF, Williams PR (2011) Excess pressure drop and drag calculations for strain-hardening fluids with mild shear-thinning: Contraction and falling sphere problems. J. Non-Newt. Fluid Mech. 166:939-950

Walters K, Webster MF (2003) The Distinctive CFD Challenges of Computational Rheology, Int. J. Numer. Methods Fluids. 43 (5) 577-596

Walters K, Tamaddon-Jahromi HR, Webster MF, Tome MF, McKee S (2009a) The Competing Roles of Extensional Viscosity and Normal Stress Differences in Complex Flows of Elastic Liquids, Korea-Aust. Rheol. J. 21 (4) 225-233

Walters K, Webster MF, Tamaddon-Jahromi HR (2009b) The numerical simulation of some contraction flows of highly elastic liquids and their impact on the relevance of the Couette correction in extensional rheology, Chem. Eng. Sci., doi: 10,1016-j.ces.2009.01.007

Wapperom P, Webster MF (1998) A second-order hybrid finite-element/volume method for viscoelastic flows. J. Non-Newt. Fluid Mech. 79:405-431

Wapperom P, Webster MF (1999) Simulation for viscoelastic flow by a finite volume/element method. Comp. Meth. Appl. Mech. Eng. 180:281-304

Webster MF, Tamaddon-Jahromi HR, Aboubacar M (2005) Time-dependent algorithm for viscoelastic flow-finite element/volume schemes. Num. Meth. Partial Diff. Equ. 21:272-296

White SA, Gotsis AD, Baird DG (1987) Review of the Entry Flow Problem - Experimental and Numerical, J. Non-Newton. Fluid Mech. 24 (2) 121-160

Wikström K, Bohlin L (1999) Extensional Flow Studies of Wheat Flour Dough. 1. Experimental Method for Measurements in Contraction Flow Geometry and Application to Flours Varying in Breadmaking Performance, J. Cereal Sci. 29 (3) 217-226

List of Tables and Figures

Figure Legends

Fig. 10. Excess pressure drop versus Deborah number; 4:1 contraction, β=0.9; a) FENE-CR, b) LPTT and c) Oldroyd-B, FENE-CR, LPTT; N_1 d) along symmetry line and e) along boundary wall for the different models

Fig. 11. Excess pressure drop (epd) for β=0.9 and β=1/9 for Oldroyd-B, FENE-CR(L=5) and LPTT(ε=0.042)

Fig. 12. Rheological material functions of the Newtonian (Δ) and Boger fluid (●) used in the study. The shear viscosity is denoted as $\eta(\dot{\gamma})$,-and the first normal stress coefficient as $\Psi_1(\dot{\gamma})$

Fig. 13. Pressure drop with increasing volumetric flow rate (Q) for Newtonian (■) and Boger fluid (●) through 15:1 contraction ratio, together with numerical Newtonian and FENE-CR, L=5 prediction (dashed lines)

Fig. 14. Total Pressure drop versus prediction, with increasing Deborah numbers, measured for a Boger fluid (experimental) through 15:1 contraction, and FENE-CR (L=3, 5, 10)

Models	**Material constants**		
	β	ϵ	L
Newtonian	1.0	-	-
Oldroyd-B	0.9	-	-
	0.1	-	-
FENE-CR	0.9	-	3
	0.9	-	5
	0.9	-	10
	0.1	-	5
LPTT	0.9	0.042	-
	0.9	0.05	-
	0.9	0.01	-
	0.1	0.042	-

Table 1. Material constants of the constitutive models: β denotes the solvent fraction, ϵ is the model parameter of the LPTT model and *L* denotes the extensibility parameter in the FENE-CR model

Model	Rheometrical functions		
	$\eta(\dot{\gamma})$	$\eta_e(\dot{\varepsilon})$	$N_1(\dot{\gamma})$
Newtonian	η_0	$3\,\eta_0$	0
Oldroyd-B	η_0	$3\beta\eta_0 + 3(1-\beta)\eta_0\left[\frac{1}{1-De\dot{\varepsilon}-2De^2\dot{\varepsilon}^2}\right]$	$2\eta_0(1-\beta)De\dot{\gamma}^2$
FENE-CR	η_0	$3\beta\eta_0 + 3(1-\beta)\eta_0\left[\frac{f_{FENE}^2}{f_{FENE}^2 - f_{FENE}De\dot{\varepsilon}-2De^2\dot{\varepsilon}^2}\right]$	$\frac{2\eta_0(1-\beta)De\dot{\gamma}^2}{f_{FENE}}$
LPTT	$\beta\eta_0 + \frac{\eta_0(1-\beta)}{f_{LPTT}}$	$3\beta\eta_0 + 3(1-\beta)\eta_0\left[\frac{f_{LPTT}^2}{f_{LPTT}^2 - f_{LPTT}De\dot{\varepsilon}-2De^2\dot{\varepsilon}^2}\right]$	$\frac{2\eta_0(1-\beta)De\dot{\gamma}^2}{f_{LPTT}^2}$

Table 2. Rheometrical functions; shear viscosity $\eta(\dot{\gamma})$, extensional viscosity $\eta_e(\dot{\varepsilon})$, and first normal stress difference $N_1(\dot{\gamma})$.

Model fluid	Polymer	Solvent
Newtonian fluid	-	6 % water in glucose syrup
Boger fluid	500 ppm PAA	6 % water in glucose syrup

Table 3. Characteristics of the model fluids

Geometry	r_0 [mm]	r_1 [mm]	H [mm]	ε_H
1	10	2.15	15	≈ 1.54
2	15	1	30	≈ 2.71

Table 4. Geometry dimensions, where r_0 is the inlet and r_1 is the outlet radius, H is the length of the contraction region and ε_H denotes the total Hencky strain

Model fluid	Zero Shear viscosity η [Pas]	Shear-thinning factor	Power law index n [dimensionless]	Flow consistency index K [Pa·s^n]	Relaxation time λ [s]
Newtonian fluid	6.4	1	1	6.6	-
Boger fluid	8.0	0.9	1	7.9	1.40

Table 5. Rheological properties of test samples

FIGURES

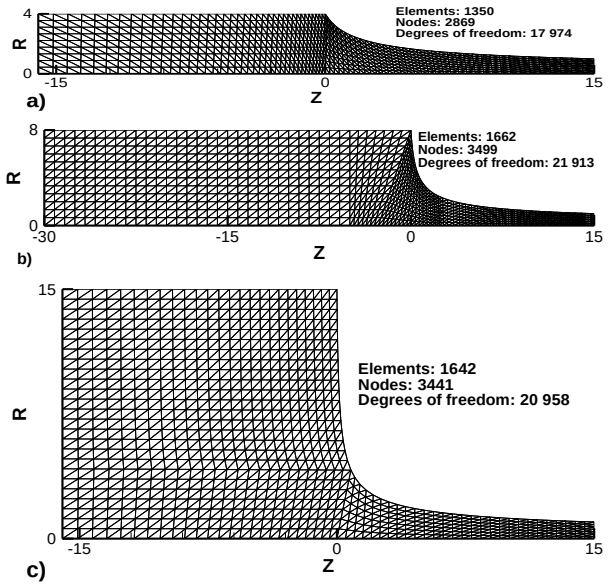

Fig. 1. Triangular mesh discretisation for axisymmetric hyperbolic: a) 4:1 contraction, b) 8:1 contraction c) 15:1 contraction with nozzle lengths of 15 ℓ

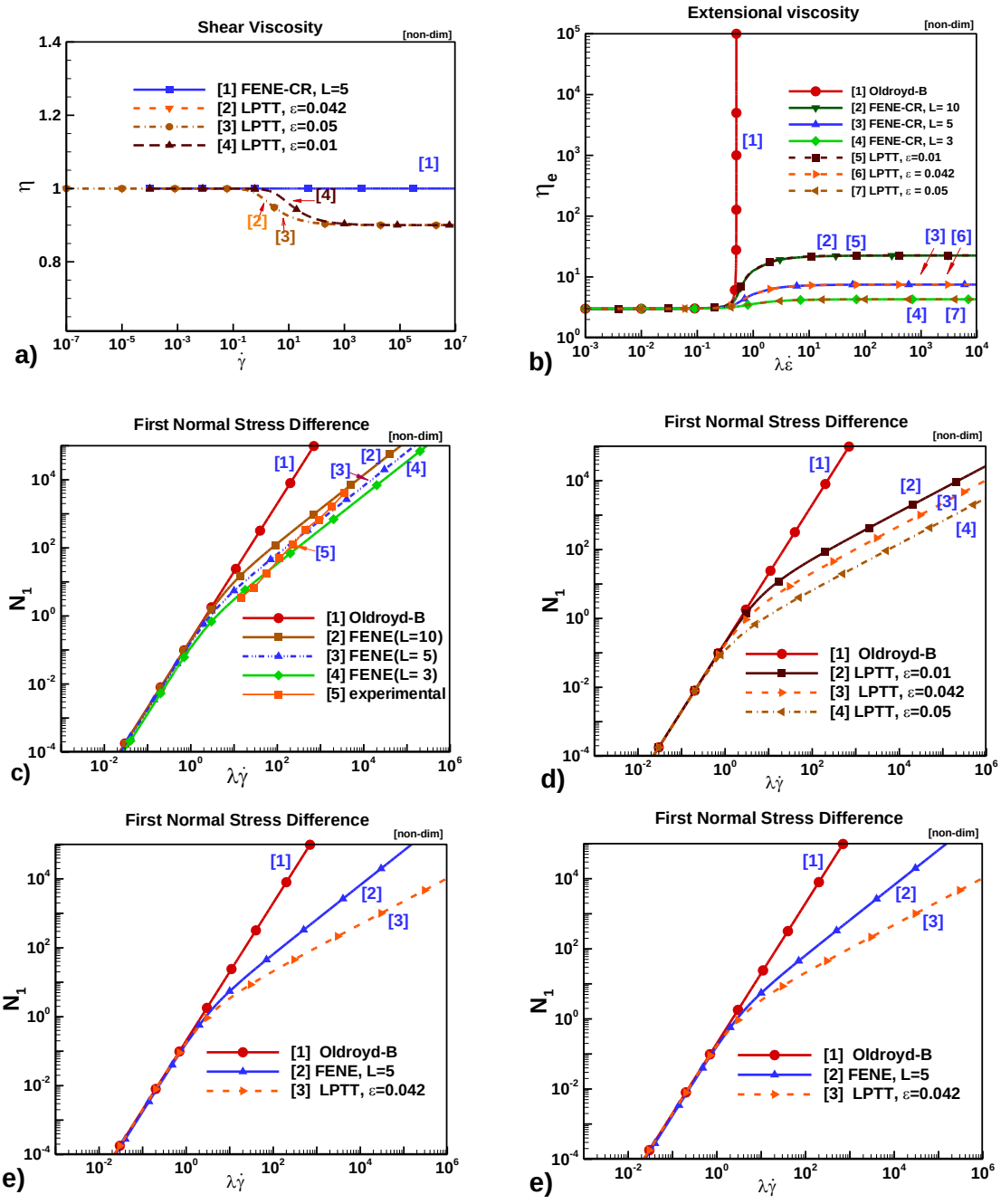

Fig. 2. Material functions: a) shear viscosity (η), b) extensional viscosity (η_e) , c-e) first normal stress difference (N_1) for different constitutive models

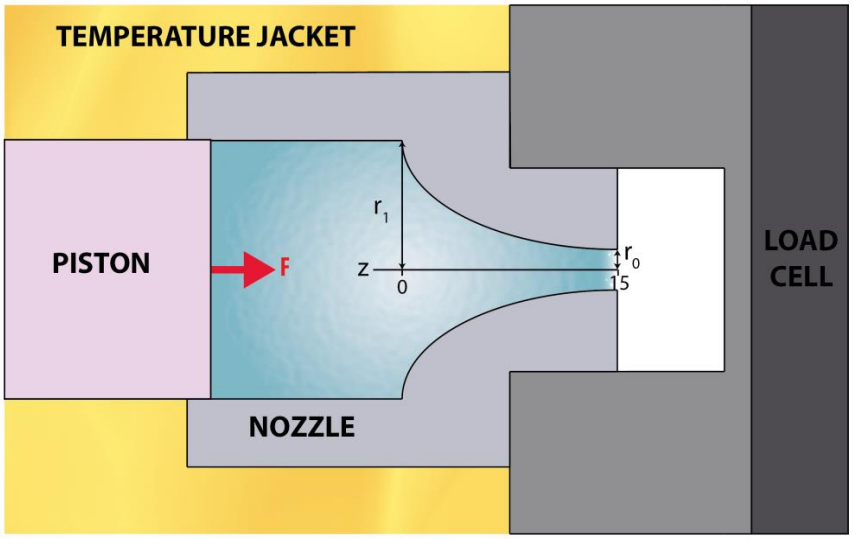

Fig. 3. Schematic diagram of the Hyperbolic Contraction Flow (HCF)

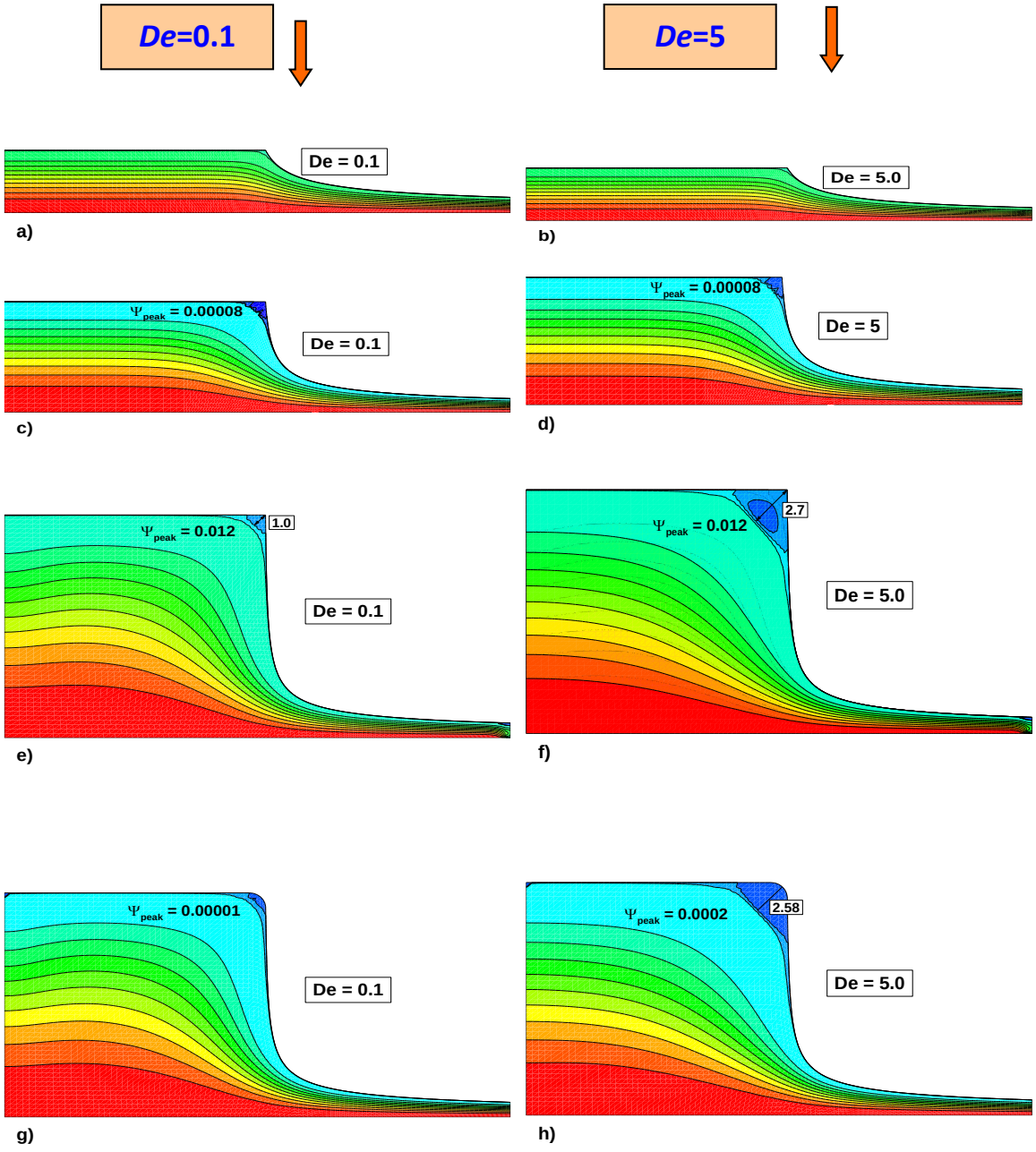

Fig. 4. Streamline patterns for the FENE-CR model, L=5 , different contraction configurations a-b) 4:1 contraction c-d) 8:1 contraction e-h) 15:1 contraction with sharp and rounded corner

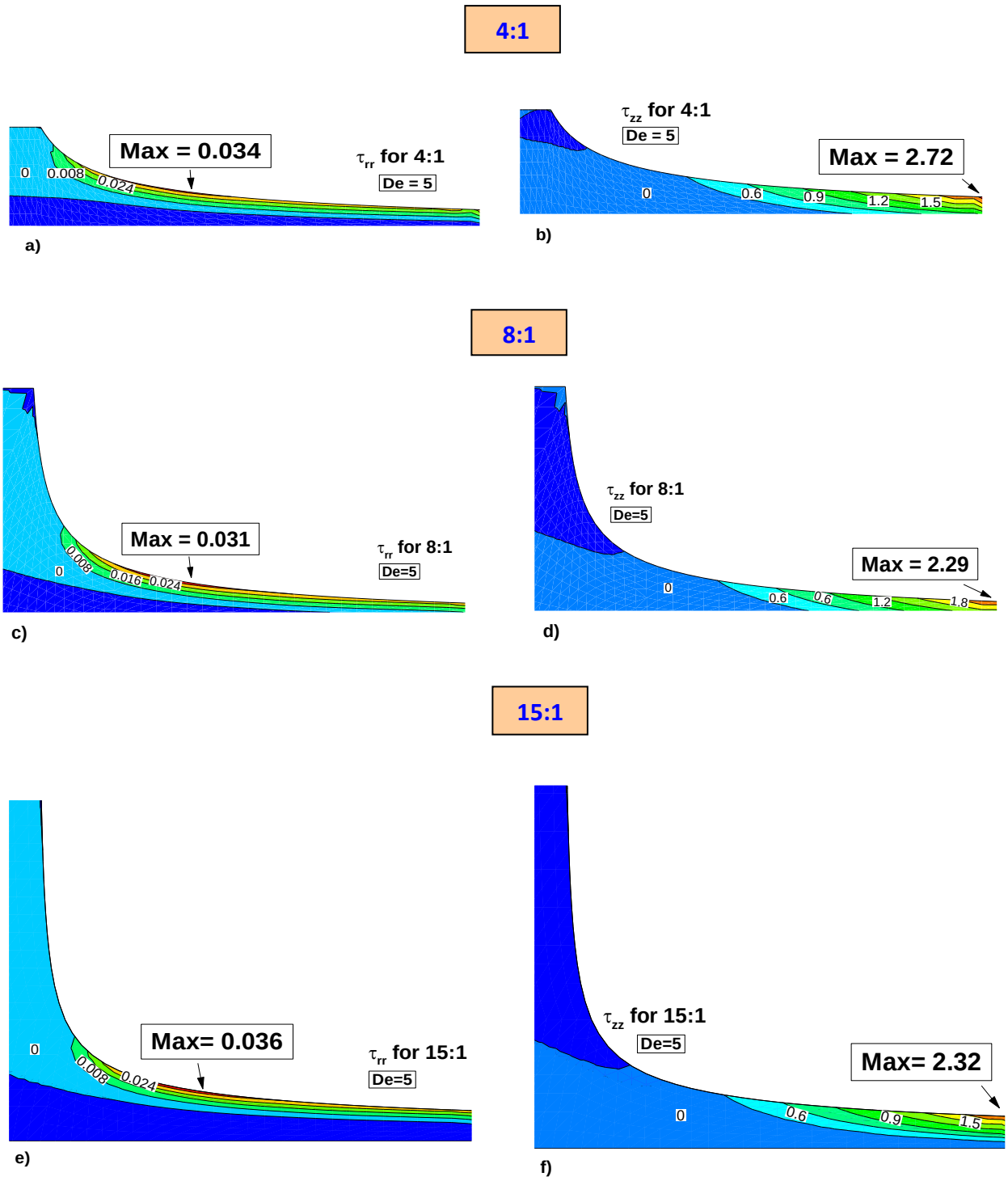

Fig. 5. Contour plots for FENE-CR, L=5, De=5 model of radial stress and axial normal stress for 4:1 a-b), 8:1 c-d), 15:1 e-f) contraction ratios

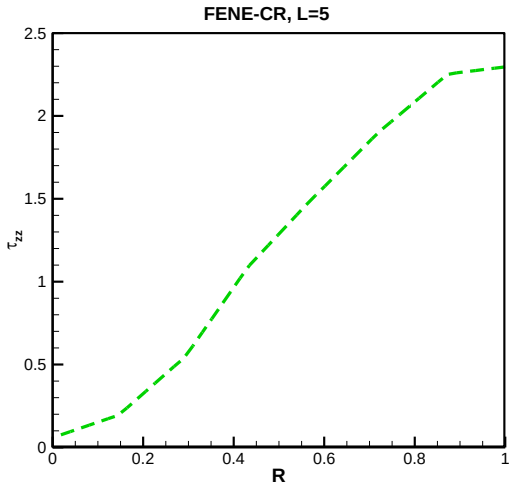

Fig. 6. Axial stress in the r-direction at a sample point of z=14.5 for FENE-CR, L=5, De=5

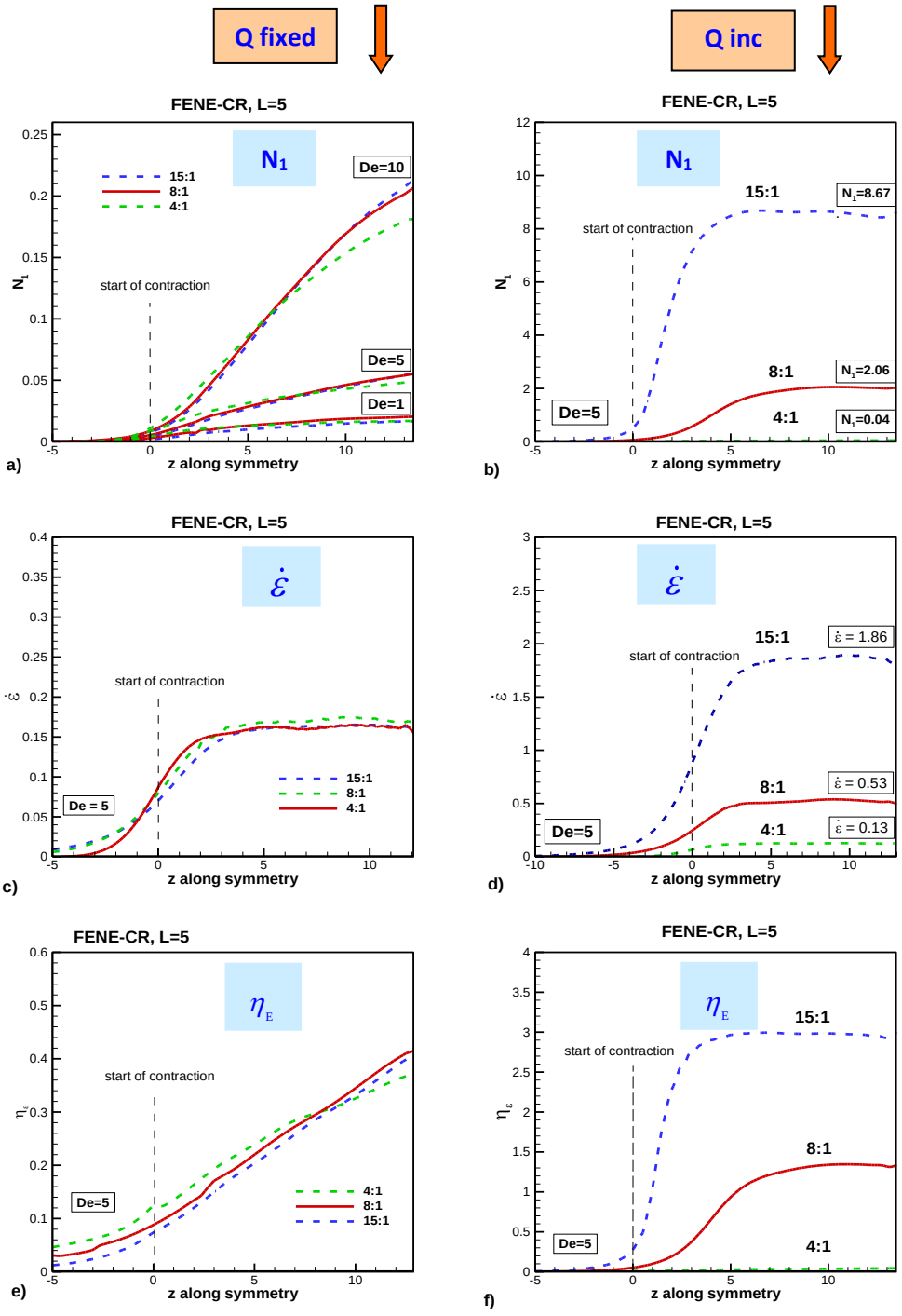

Fig. 7A. In extension, z along symmetry centreline: First normal stress difference $\mathrm{N}_1(\dot{\varepsilon})$, strain rate $\dot{\varepsilon}$ and extensional viscosity $\eta(\dot{\varepsilon})$ are displayed, for three different contraction ratios; fixed flow rate (a,c,e) and increasing flow rate (b,d,f); FENE-CR(L=5)

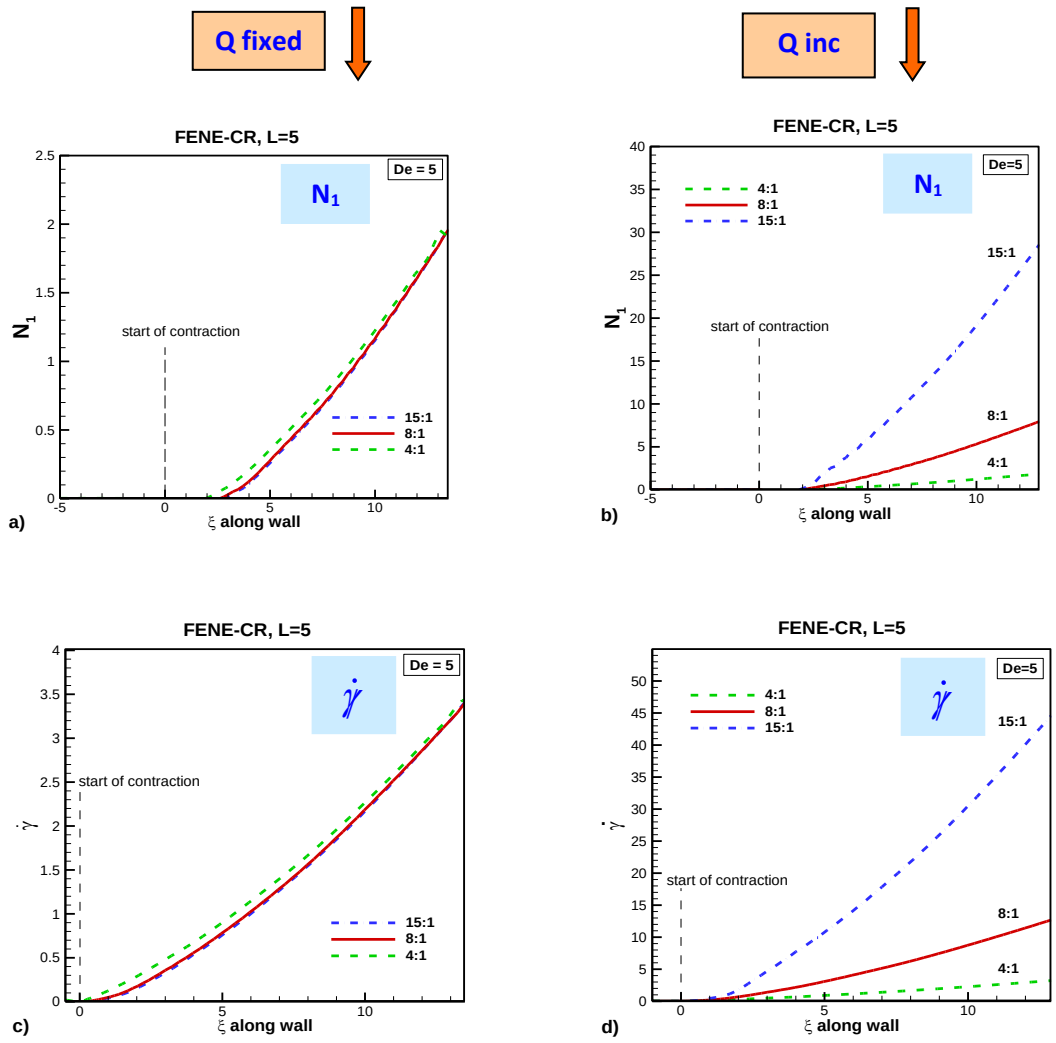

Fig. 7B. In shear, z along boundary wall: First normal stress difference $N_1(\dot{\gamma})$ and shear rate $\dot{\gamma}$ are displayed, for three different contraction ratios; fixed flow rate (a,c) and increasing flow rate (b,d); FENE-CR(L=5)

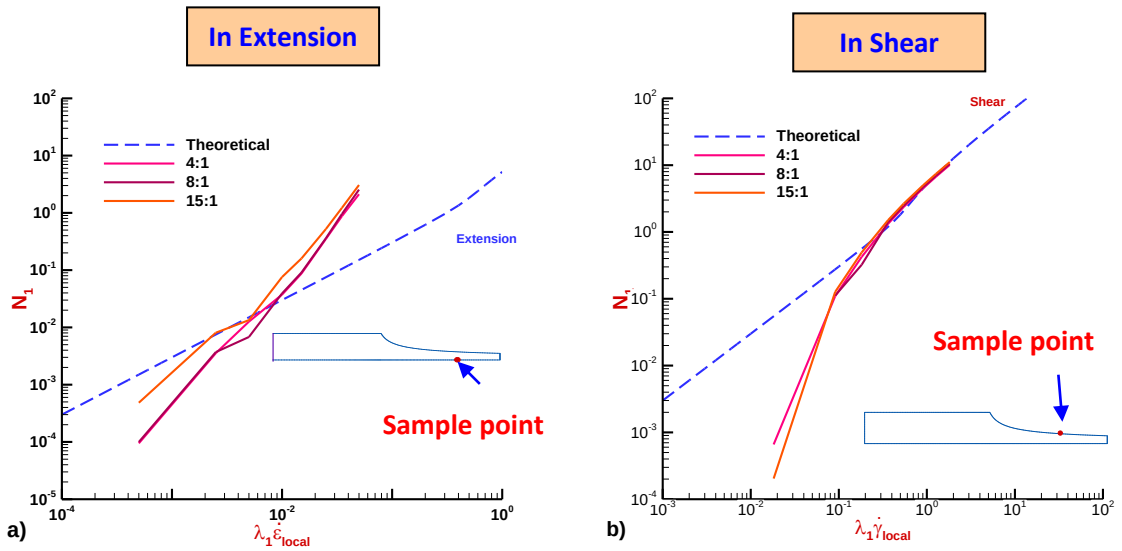

Fig. 8. In extension a) and shear b): First normal stress difference for FENE-CR (L = 5) for contraction ratios of 4:1, 8:1 and 15:1 fixed Q, increasing De taken at sample points z=9 compared to theoretical values

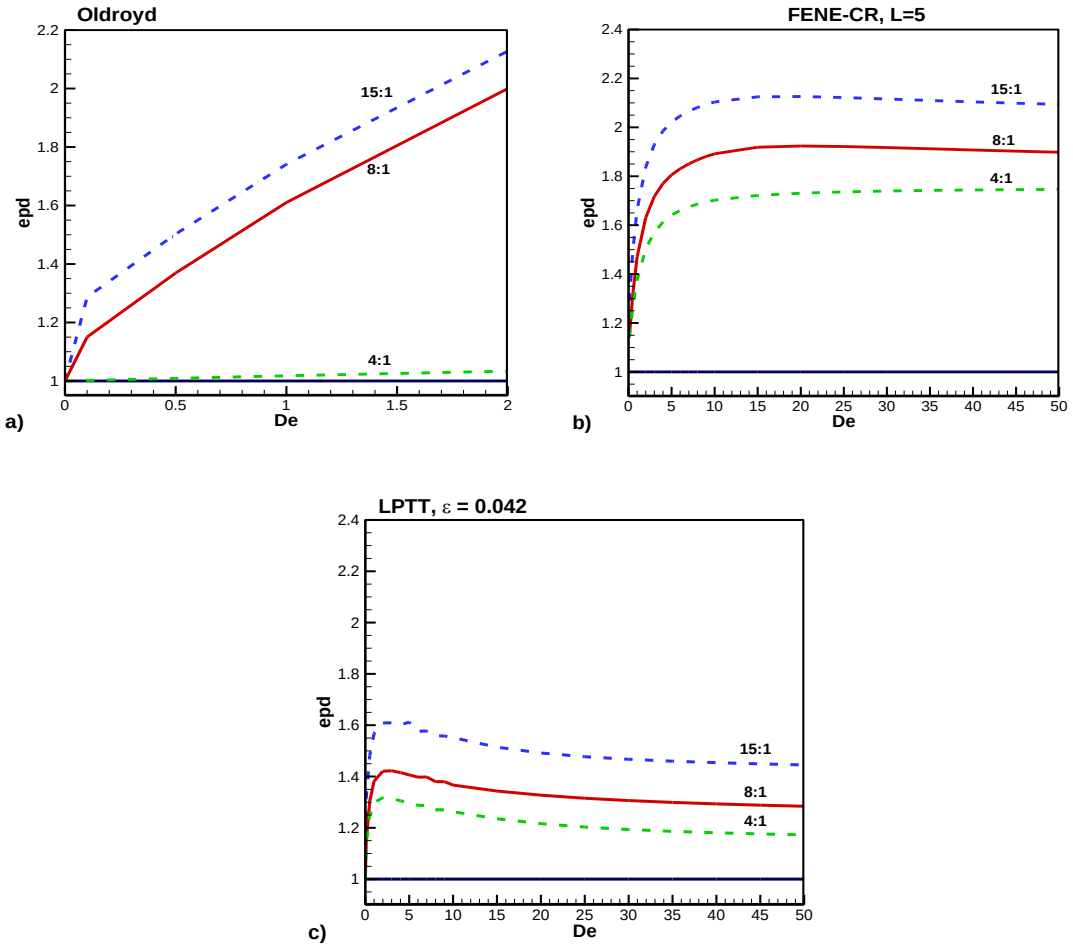

Fig. 9. Comparison of excess pressure drop (epd) results for different contraction ratios for β=0.9 a) Oldroyd-B, b) FENE-CR, L=5 and c) LPTT, ε=0.042

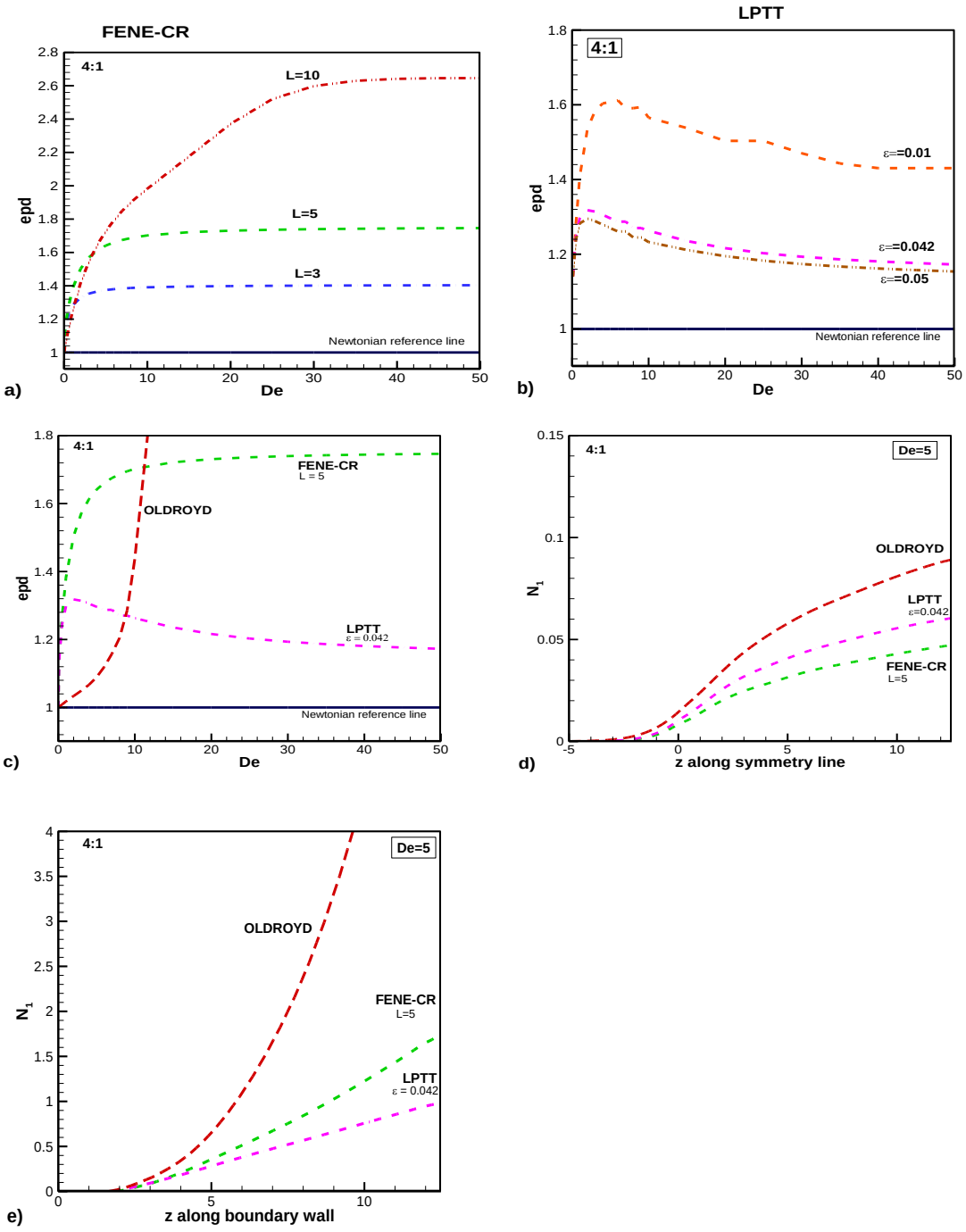

Fig. 10. Excess pressure drop versus Deborah number; 4:1 contraction, β=0.9; a) FENE-CR, b) LPTT and c) Oldroyd-B, FENE-CR, LPTT; N_1 d) along symmetry line and e) along boundary wall for the different models

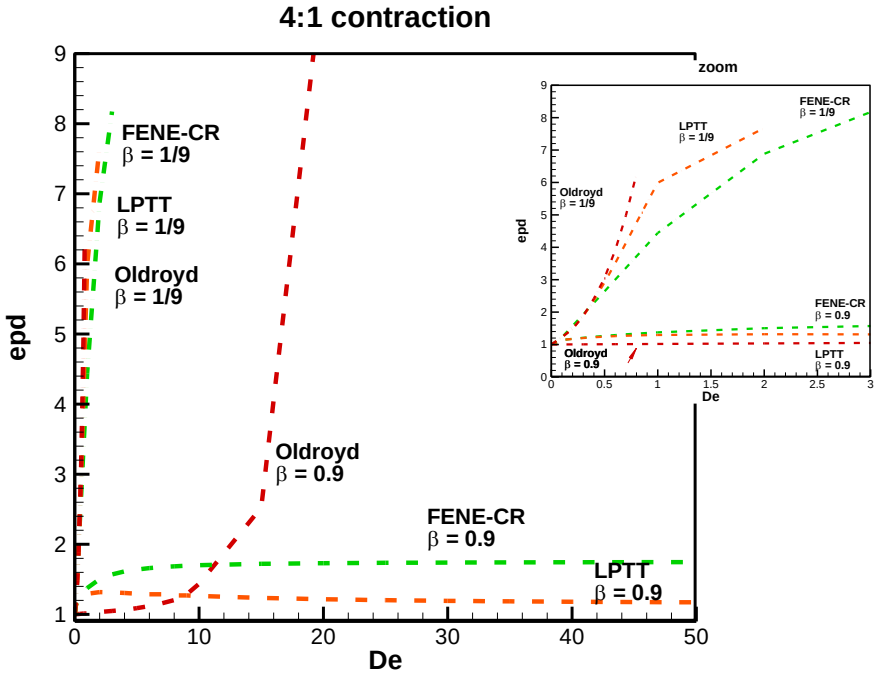

Fig. 11. Excess pressure drop (epd) for β=0.9 and β=1/9 for Oldroyd-B, FENE-CR(L=5) and LPTT(ε=0.042)

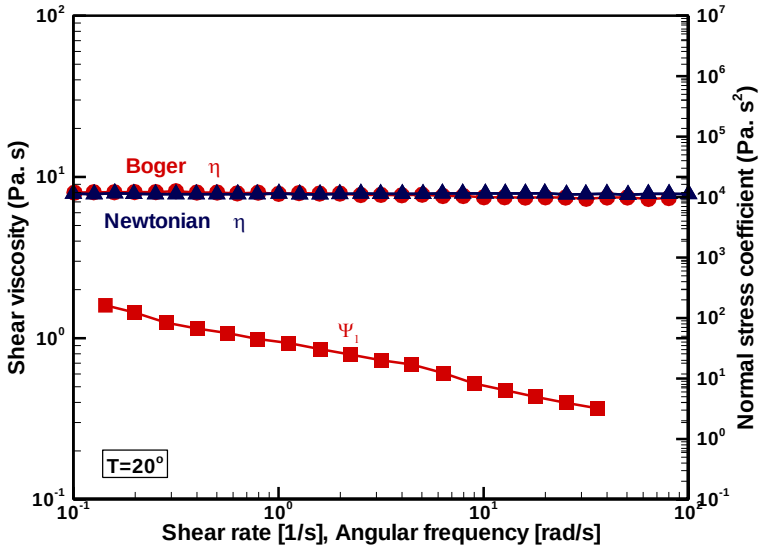

Fig. 12. Rheological material functions of the Newtonian (Δ) and Boger fluid (●) used in the study. The shear viscosity is denoted as $\eta(\dot{\gamma})$, and the first normal stress coefficient as $\Psi_1(\dot{\gamma})$

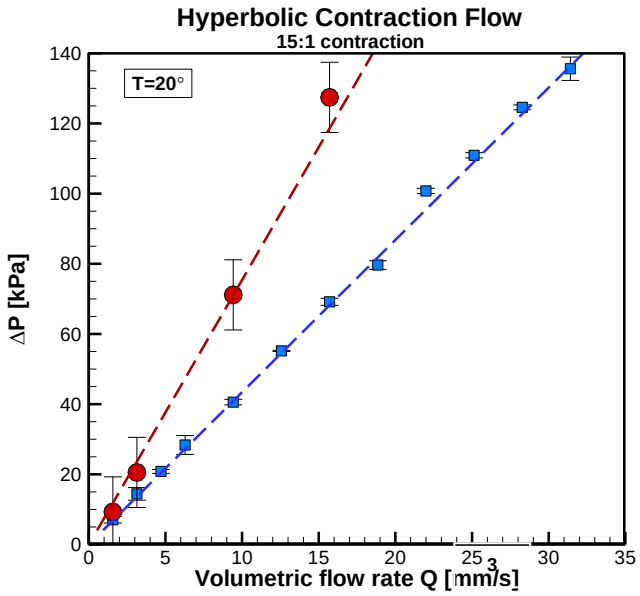

Fig. 13. Pressure drop with increasing volumetric flow rate (Q) for Newtonian (■) and Boger fluid (●) through 15:1 contraction ratio, together with numerical Newtonian and FENE-CR, L=5 prediction (dashed lines)

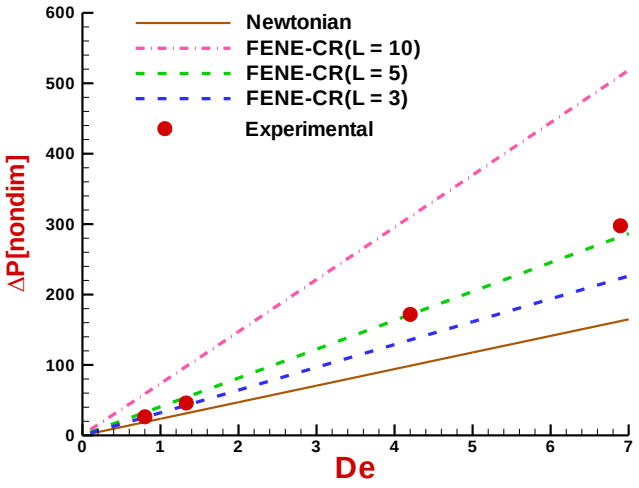

Fig. 14. Total Pressure drop versus prediction, with increasing Deborah numbers, measured for a Boger fluid (experimental) through 15:1 contraction, and FENE-CR (L=3, 5, 10)